SI Appendix

Nitrogenase-mimic Iron-containing chalcogels for photochemical reduction of dinitrogen to ammonia

Jian Liu[a,b], Matthew S. Kelley[a,b], Weiqiang Wu[a,b], Abhishek Banerjee[a,b], Alexios P. Douvalis[c], Jinsong Wu[a,b], Yongbo Zhang[a,b], George C. Schatz[a,b,1], Mercouri G. Kanatzidis[a,b,1]

[a]Department of Chemistry, Northwestern University, Evanston, Illinois 60208; [b]Argonne-Northwestern Solar Energy Research Center, Northwestern University, Evanston, Illinois 60208; [c]Department of Physics, University of Ioannina, 45110 Ioannina, Greece

[1]To whom correspondence may be addressed. E-mail: g-schatz@northwestern.edu; m-Kanatzidis@northwestern.edu

Methods

Chalcogel precursor synthesis.

All manipulations were performed in a N_2 atmosphere glovebox. $(NBu_4)_3[Mo_2Fe_6S_8(SPh)_3Cl_6]$ (Cluster **1**) was synthesized as follows: **1)** 40 mmol (5.28 g) of Sodium thiophenolate was dissolved in 40 mL methanol with stirring. To this solution was added a solution of 10 mmol (1.62 g) $FeCl_3$ in 20 mL methanol; **2)** The above solution was stirred for 30 minutes, and then 3.3 mmol (0.87 g) of $(NH_4)_2MoS_4$ was added; **3)** The reaction mixture was then stirred overnight, and then filtered into a methanolic solution of NBu_4Br (10 mmol, 3.22 g in 20 mL methanol). A black precipitate forms, which is vacuum filtered and allowed to dry; **4)** The crude product is then recrystallized by dissolution in warm acetonitrile (~40 mL at 60°C) and filtered immediately and finally 200 mL of methanol is added to the above warm acetonitrile solution; **5)** After 3-4 days standing, pure black platelike crystals are obtained, which are filtered, washed with methanol, and dried under vacuum; **6)** $(NBu_4)_3[Mo_2Fe_6S_8(SPh)_9]$ is converted into the cluster $(NBu_4)_3[Mo_2Fe_6S_8(SPh)_3Cl_6]$ (cluster **1**) by the addition of benzoyl chloride (PhCOCl, ~400 μL) into a solution of 2530 mg of $(NBu_4)_3[Mo_2Fe_6S_8(SPh)_9]$ in acetonitrile, followed by stirring for 3-4 hours at elevated temperature (50°C) and precipitation with a large excess (~ 400 mL) of ether after overnight standing.

$(Ph_4P)_2[Fe_4S_4Cl_4]$ (Cluster **2)** was synthesized as follows: **1)** 1.0 g of $FeCl_2$ (7.89 mmol), 1.56 g of NaSPh (11.80 mmol), 1.48 g of Ph_4PCl (3.94 mmol), and 0.32 g of S (9.86 mmol) were dissolved in 40 mL acetonitrile and stirred for 1.5 hours at room temperature; **2)** The brown solution was filtered, and 200 mL of ether was added to the filtrate and allowed to stand overnight; **3)** Then, the solution was filtered and washed with ether, yielding a black crystalline product; **4)** These black crystals were re-dissolved in acetonitrile and filtered to collect the filtration; **5)** An excess of ether was added to the resulting amber-brown solution and again allowed to stand overnight; **6)** The resulting black crystals were filtered, washed with ether, and allowed to dry under nitrogen.

The $Na_4Sn_2S_6{\cdot}14H_2O$ (Cluster **3)** was synthesized using a modification of the literature method as follows: **1)** 60 mmol of $Na_2S{\cdot}9H_2O$ (14.4 g) was dissolved in 100 mL of water with vigorous stirring; **2)** 15 mmol (5.2 g) of $SnCl_4{\cdot}5H_2O$ is dissolved in 5 mL water and continuously added to the Na_2S solution with vigorous stirring. Yellow flakes form upon addition of the $SnCl_4$, and control the addition speed to be sure that yellow flakes are always present, which eventually dissolve to form a transparent yellow solution; **3)** The clear yellow solution is then slowly added to 300 mL acetone with vigorous stirring. The acetone solution goes from clear to blue to green, and ultimately viscous yellow oil is seen on the bottom of the flask with a white translucent solution on top. The flask is placed in a refrigerator at -20°C for 2 days; 4) The top transparent layer is decanted away, and 100 mL of acetone is added to the yellow oil with vigorous stirring. The mixture is then manually shaken until a white precipitate forms; 5) The flask is placed back into the refrigerator for another 24 h, and then the precipitate is collected, filtered, washed with acetone, and dried under mild vacuum in the fume hood.

Chalcogel Synthesis.

Chalcogel synthesis was performed in a N_2 atmosphere glovebox. The detailed procedure is as follows:

1) In a typical synthesis, 100 mg (~0.12 mmol) of $Na_4Sn_2S_6{\cdot}14H_2O$ was dissolved in 1 mL of N-methylformamide in a scintillation vial; **2)** In a separate vial, 250 mg (~0.12 mmol) of Cluster

1, 2 or 1&2, or 1&inert ions was dissolved in 1 mL of N, N-dimethylformamide, respectively; **3)** This solution was then slowly added to the $Na_4Sn_2S_6 \cdot 14H_2O$ solution. The $Na_4Sn_2S_6$ solution is shaken manually during addition. When the addition is complete, a viscous black liquid results. This liquid is left undisturbed at room temperature for one week. At that time, the viscous liquid has completely solidified into a black gel; **4)** The gel is subjected to cleaning by solvent exchange with a 4:1 (v:v) mixture of ethanol and water (4x), followed by pure ethanol (3x). The solvent is exchanged every 24 hours, so that the entire cleaning procedure took about a week.

Chalcogel Characterizations.

Scanning Electron Microscopy was performed on a Hitachi S4800N-II instrument equipped with an energy dispersive spectroscopy (EDS) detector. Transmission Electron Microscopy was performed on a Hitachi 8100 instrument. A critical point drying apparatus (Tousimis Autosamdri 815B Series A) was used to remove the solvent from the solvent-exchanged chalcogels. Slices of the chalcogel were placed into the critical point dryer, and the chamber was cooled with liquid carbon dioxide to 0 °C. Liquid CO_2 was then introduced into the chamber to exchange out the remaining ethanol solvent. Fresh liquid CO_2 was introduced into the chamber every 20-30 minutes over the course of 7-8 hours in order to completely remove all traces of ethanol. Then, the supercritical drying was done at elevated temperature and pressure (41 °C, 1400 psi) for 4 minutes, followed by the gaseous CO_2 being slowly bled out of the chamber. The aerogels are then immediately placed under nitrogen to minimize oxidation from the air, and can then be used for surface area measurements by nitrogen adsorption. The aerogels are placed in a sample tube and degassed at 75 °C under vacuum overnight. Nitrogen adsorption/desorption isotherms were obtained at 77 K on a Micromeritics ASAP 2020 instrument. The surface area was measured using the Brunauer-Emmett-Teller (BET) model using a series of relative pressures P/P^0 from 0.05-0.30. For thiol extrusion studies: 30 mg of dried gel was suspended in 9 mL of DMF following with addition of 1 mL of HSPh, leading to a dark brown colored solution. UV-Vis spectroscopy was employed to characterize the absorbance of the diluted solution at 455 nm.

Cyclic Voltammetry.

In a conventional three-electrode setup using Chi 900B Potentiostat, Pt wire and Ag/AgCl were used for the counter and reference electrodes respectively. A 0.1M tetrabutylammonium hexafluorophosphate in acetonitrile flushed with N_2 gas was used as an electrolyte solution. The slices of wet chalcogel were placed on the surface of the working electrode (glassy carbon electrode) by packing them with a blade gently. The electrolyte was then introduced to the cell carefully so that the chalcogels were stable on the surface of the electrode.

Supplement description of the main text.

The morphological and structural characterizations of FeMoS-SnS, FeS-SnS, FeMoS-Sb-SnS, FeMoS-Sn-SnS, and FeMoS-Zn-SnS chalcogels were illustrated in SI Appendix, Fig. S4-7, respectively. The similar morphologies and comparable surface area suggested that the incorporation of a third component (Fe_4S_4, Sb^{3+}, Sn^{4+}, Zn^{2+}) does not change the structural properties of the biomimetic chalcogels comparing with original FeMoS-SnS chalcogel. The schematic illustration of FeS-SnS gel linked by Sn_2S_6 is shown in SI Appendix, Fig. S5a. The SEM image of FeS-SnS in SI Appendix, Fig. S6b indicates the typical morphology of the chalcogel. TEM in SI Appendix, Fig. S5c demonstrates porosity of the FeS-SnS chalcogel also lacking of long-range order and selected area electron diffraction indicated amorphous property

of the chalcogel. The FeS-SnS gel featured large surface area 148 m^2/g, which might contribute to the more active sites for N_2 adsorption and binding (SI Appendix, Fig. S5d). The Mössbauer spectrum of the FeS-SnS gel recorded at 77 K, as shown in SI Appendix, Fig. S5e, is composed of a quadrupole split part, which was fitted using a combination of two components of equal areas. The resulting Mössbauer parameters (IS_1=0.45 mm/s, IS_2=0.45 mm/s and QS_1=0.65 mm/s, QS_2=1.12 mm/s) are indicative of the Fe_4S_4 cluster.[1]

Usually, proton and electron sources are simultaneously required for catalyzing conversion of N_2 to ammonia.[2] Hydrogen and NADH (Nicotinamide adenine dinucleotide, reduced form) were employed as the potential hydrogen and electron donors, respectively. However, in such cases, no ammonia could be obtained in the presence of FeMoS-FeS-SnS chalcogel, which suggested its different behavior from industrial Haber-Bosch Iron catalyst or nitrogenase (SI Appendix, Table S3, entry 6-7). Based on our group's previous work, NaAc and PyrH were chosen to act as electron and proton sources, respectively.[3] Without either of two, production of ammonia was impossible, which further confirmed the standard condition. However, when both NaAc and PyrH were replaced with 5 mM L-ascorbic acid (abbreviated as L-AA, and pH of starting reaction solution equals to ca. 3.4), some ammonia (2.5 ppm) was detected. In such case, L-AC was thought to act as both electron donor and proton donor to accomplish N_2 reduction. When we used L-AA as the equivalent of NaAc and PyrH, 55 mM of L-AA was added to the reaction solution. In such a case, only slightly higher ammonia production was obtained. However, too much L-AA (110 mM, pH=2.8) will harm the photocatalytic performance, and only trace amount (1 ppm) of ammonia could be obtained (SI Appendix, Table S3, entries 9-11). Further incorporation of 5 mM L-AA and 50 mM PyrH (pH=3.1) gave greater performance (10.2 ppm), as also illustrated in SI Appendix, Fig. S9a. This suggests that the combination of L-AA and PyrH gives slightly better performance than that of NaAc and PyrH combination. The inferior results in the presence of only L-AA also implicated that pyridine might play role beyond proton donor. As it's well known that pyridine or the intermediate dihydropyridine could catalyze the CO_2 reduction in heterogeneous and homogeneous solutions,[4-6] we speculate the pyridine herein might also contribute to the N_2 reduction beyond the proton donor role. Further analysis is still needed to elucidate the real role of the pyridine. The common electron mediator I^- was also combined with PyrH and 1 ppm of NH_4^+ was induced to form (See SI Appendix, Table S3, entries 12-13). Further identifying more optimal electron and proton donor combinations are underway.

Control experiments were performed on DRIFTS. The bands at 1753 or 1746 cm^{-1} do not appear without both light irradiation and flow of N_2 (SI Appendix, Fig. S12). No changes could be observed in the DRIFTS spectra under Argon atmosphere for the FeMoS-FeS-SnS aerogel sample in either dark or light conditions. The control experiments clearly suggested the newly formed bands at 1753 and 1746 cm^{-1} originated from *in situ* light reactions with N_2.

Broken Symmetry DFT Calculations.

As described earlier, high spin solutions for the model complexes (SI Appendix, Fig. S14) were calculated for each oxidation state. Then, different combinations of spin flips were performed on all of the open shell metal centers. For the MoFeS cluster, because the exact oxidation state of each metal was unknown and the large number of possible combinations of spin flips that could be performed, we restricted ourselves to only investigating combinations that would lead to an overall $M_s = 0$ or $M_s = 3$ for the 3- oxidation state and $M_s = 0$ or $M_s = 4$ for the 5- oxidation state, in accordance with past magnetic measurements made on the complexes.[7]

Lowest energy solutions were selected and geometry optimizations were performed for these combinations. The lowest energy solution for each oxidation state involved the same sequence of spin flips outlined in SI Appendix, Fig. S15. For the Fe_4S_4 cluster, optimal combinations of spin flips were found in the same manner, though all of the possible combinations could be explored due to the small combination space involved in four iron atoms. All calculations were performed with the TPSSh functional[8] using the relativistically contracted Karlsruhe def2-TZVP basis sets[9,10] with the RIJCOSX approximation[11-13] and ZORA approximation.[14,15] All calculations also included aqueous solvent effects using the COSMO solvation model[16] and account for dispersion forces with the DFT-D3BJ dispersion correction of Grimme.[17,18] For nitrogen binding, several configurations were tested with various Fe and Mo centers as the binding site. The only stable configurations occurred between nitrogen and molybdenum or nitrogen and iron when a chloride ligand was released. The energy of reduction in Fig. 6 was computed by calculating the energy difference between the ascorbate ion and its radical form and adding this difference to the difference between the complex and its reduced form. Similarly, proton energies were computed by factoring in the difference in energy between pyridinium and its deprotonated form, pyridine. These molecules were optimized using the same functional, basis sets, and other approximations as used in the broken symmetry calculations; their energies are compiled in SI Appendix, Table S4.

Table S1. Summary of the reported examples of photochemical N_2 fixation in the literatures and this work.

Entry	Catalyst system	Irradiation light	Eg (eV)	NH_4^+ concentration (ppm)	Reaction time (h)	Detection method	Sacrificial agent	References
1	Fe/TiO_2	Hg arc lamp	3.2	0.1 ppm (20 ml*)	3	Colorimetric method by Kruse and Mellon	H_2O	*J. Am. Chem. Soc.*, **1977**, 99 (22), 7189-7193
2	$Fe_2Ti_2O_7$	λ >320 nm	2.9[19]	0.306 ppm (32 mL)	24	Colorimetric method by Kruse and Mellon	CH_3CH_2OH	*Angew. Chem. Int. Ed.* **2001**, 40, 3993-3995.
3	Au/Nb-$SrTiO_3$/Ru	800 nm>λ>550 nm	3.2	0.72 ppm (0.2 ml)	24	Indophenol method	CH_3CH_2OH+HCl	*Angew. Chem. Int. Ed.* **2014**, 53, 9802-9805
4	Diamond	λ >190 nm	5.5	0.8 ppm (10 ml**)	24	Indophenol method	KI	*Nat. Mater.* **2013**, 12, 836-841
5	BiOBr-ov	λ > 420 nm	2.8	1.08 ppm (100 ml)	1	Nessler's Reagent	H_2O	*J. Am. Chem. Soc.*, **2015**, 137, 6393-6399
6	FeMoS-SnS Chalcogel	λ >190 nm	0.9	5.3 ppm	48	Indophenol method	PyrH and NaAc	*J. Am. Chem. Soc., **2015**, 137, 2030–2034*
7	FeMoS-FeS-SnS chalcogel	λ >190 nm	0.7	10.5	48	^{1}H NMR	PyrH and NaAc	*This work*
8	FeS-SnS chalcogel	λ >190 nm	NA***	16	48	^{1}H NMR	PyrH and NaAc	*This work*

***** The volume is not indicated in the paper. We assume 10 ml of the reaction solution for calculation of ppm concentration.

****** The volume is not indicated in the paper. We assume 10 ml of the reaction solution for calculation of ppm concentration.

******* Fe_4S_4 aerogel is extremely air-sensitive and the diffuse reflectance spectrum of this gel can't be obtained under ambient experimental condition.

Table S2. Synthetic parameters and the empirical formula of the chalcogels.

	Composition 1		Composition 2	Gelation status	Empirical formula	M_W	Solid content in wet chalcogel%*
	$Mo_2Fe_6S_8$ in DMF	M in DMF	$Na_4Sn_2S_6$ in NMF				
FeMoS-SnS	0.12 mmol	0	0.12 mmol	✓	$Na_5[Mo_2Fe_6S_8(SPh)_3](Sn_2S_6)_3$	2516	12
FeMoS-FeS-SnS	0.06 mmol	0.06 mmol	0.12 mmol	✓	$NaP_{2.2}[Mo_2Fe_6S_8(SPh)_3][Fe_4S_4](Sn_2S_6)_{2.2}$	3180	0.12
FeMoS-Sb-SnS	0.06 mmol	0.06 mmol	0.12 mmol	✓	$Na_6[Mo_2Fe_6S_8(SPh)_3](Sn_2S_6)_5Sb_2$	3643	0.11
FeMoS-Sn-SnS	0.06 mmol	0.06 mmol	0.12 mmol	✓	$Na_4[Mo_2Fe_6S_8(SPh)_3](Sn_2S_6)_6Sn_2$	4021	0.14
FeMoS-Zn-SnS	0.06 mmol	0.06 mmol	0.12 mmol	✓	$Na_5[Mo_2Fe_6S_8(SPh)_3](Sn_2S_6)_5Zn_2$	3506	0.13
FeS-SnS	0	0.12 mmol	0.12 mmol	✓	$Na_{1.2}[Fe_4S_4](Sn_2S_6)_{2.5}$	1455	0.12

*Solid mass left after drying the wet chalcogel was used to determine that moles of catalyst used.

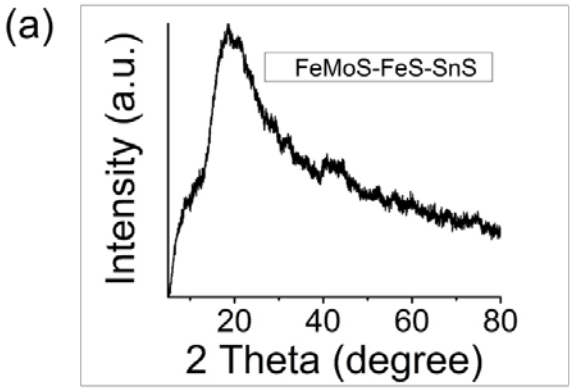

(b)

	IS1	QS1	IS2	QS2	Area %
Component 1	0.44	0.76	0.43	1.17	0.48
Component 2	0.47	0.62	0.49	1.13	0.48
Component 3	1.28	2.93	1.03	2.44	0.04

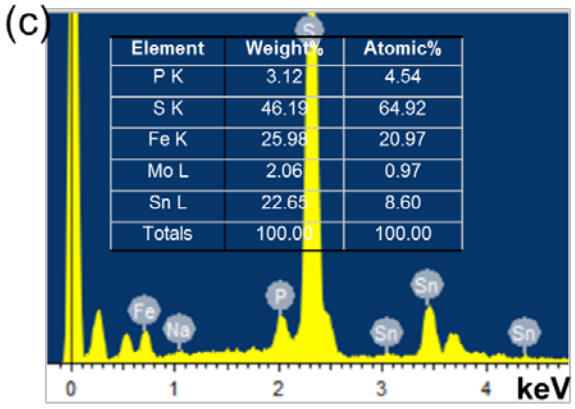

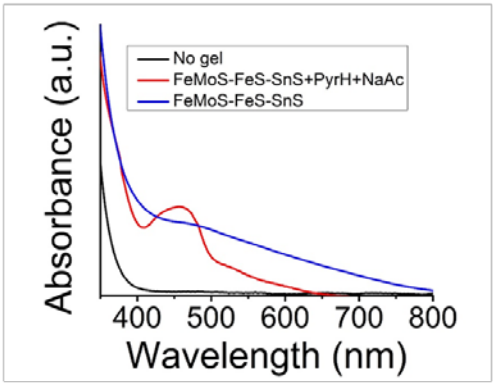

Figure S1. (a) XRD pattern of FeMoS-FeS-SnS chalcogel, indicating the amorphous property. (b) Mössbauer spectrum of the FeMoS-FeS-SnS chalcogel recorded at 77 K and the corresponding parameters obtained from the Mössbauer measurement. (c) Typical energy-dispersive spectrum of FeMoS-FeS-SnS chalcogel. The inset table in panel e indicates the atom and weight ratio in FeMoS-FeS-SnS chalcogel. (d) UV-vis spectra of FeMoS-FeS-SnS chalcogels that have been exposed to excess benzenethiol in the absence (blue) and presence of PyrH and NaAc, respectively.

Table S3. Summaries of the photochemical N_2 fixation results.

Entry	e^-	H^+	Nitrogen source	Yield (ppm)
1*	NaAc	PyrH	$^{14}N_2$	8.3
2**	NaAc	PyrH	$^{14}N_2$	4.1
3***	NaAc	PyrH	$^{14}N_2$	0
4****	NaAc	PyrH	$^{14}N_2$	0
5	NaAc	PyrH	Pressured N_2	7
	e^-	H^+	pH	Yield (ppm)
6	H_2		7	0
7	NADH		7	NA
9	5 mM Ascorbic Acid		3.4	2.5
10	55 mM Ascorbic acid		3.2	3.4
11	110 mM Ascorbic acid		2.8	1.0
12	5 mM Ascorbic acid	PyrH	3.1	10.2
13	KI	PyrH	4	1

* Standard condition
** Equipped with 420 nm filter
*** No light
**** No chalcogel

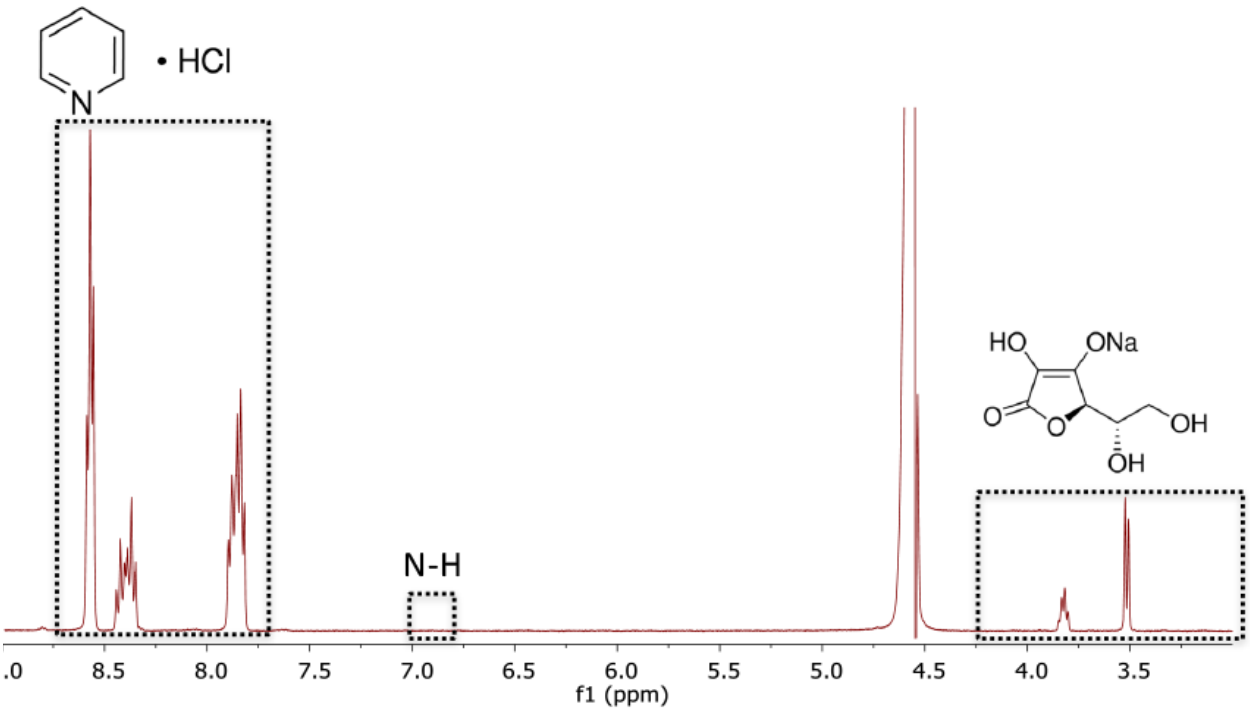

Figure S2. ^{1}H NMR of the starting reaction solution with 10% DMSO-d_6. The rectangular frames indicate the corresponding sacrificial agents.

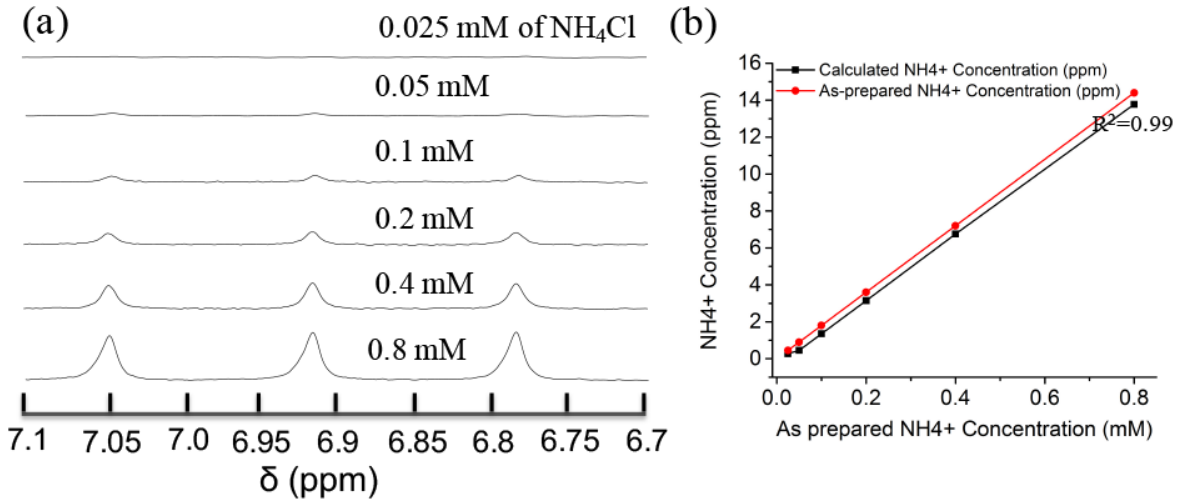

Figure S3. (a) ^{1}H NMR of a series of authentic $^{14}NH_4Cl$ sample with different concentrations. (b) $^{14}NH_4Cl$ authentic sample calibration curve on ^{1}H NMR.

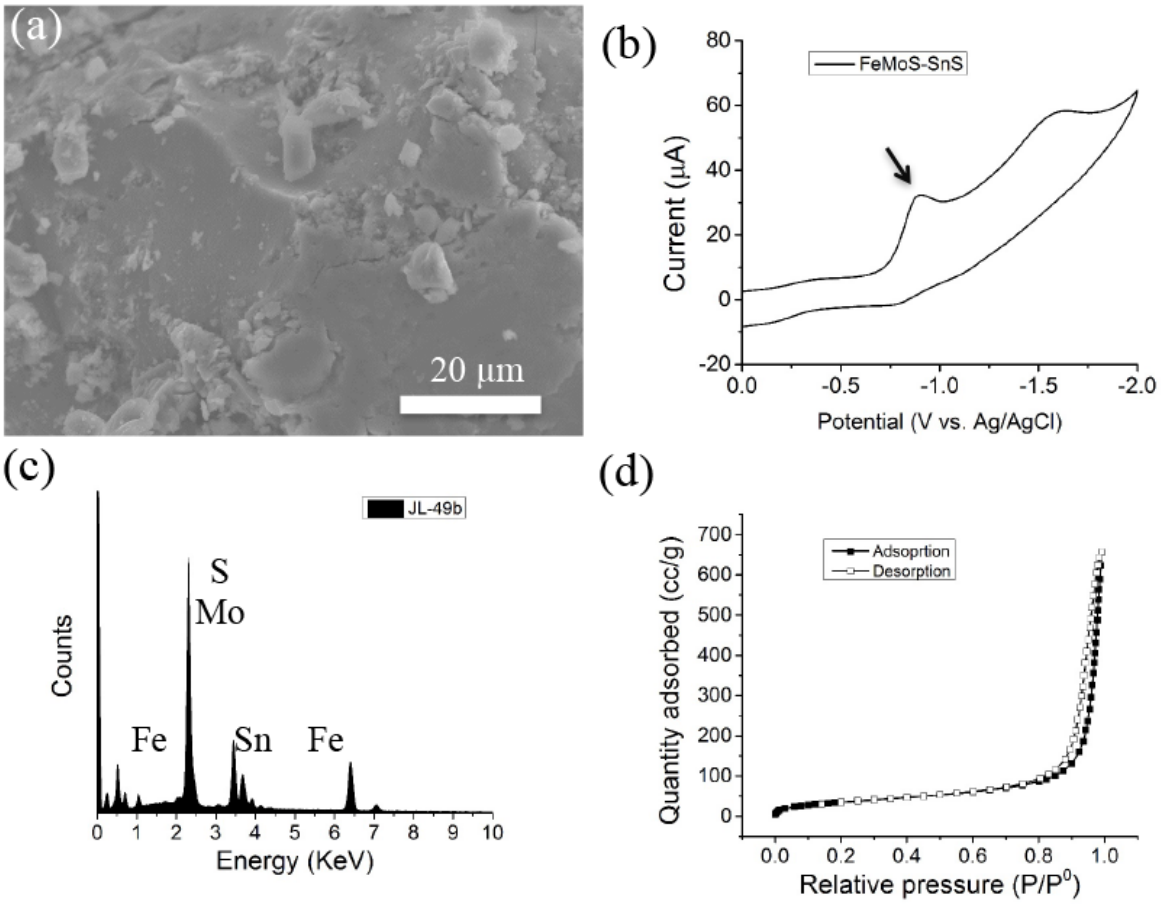

Figure S4. Characterizations of FeMoS-SnS Chalcogel. (a) SEM images with different magnifications. (b) Cyclic voltammetry of FeMoS-SnS chalcogel at 50 mV/s scan rate with first reduction peak at -0.89 V. (c) EDX spectra of FeMoS-SnS chalcogel. (d) N_2 adsorption-desorption isotherms of FeMoS-SnS aerogel.

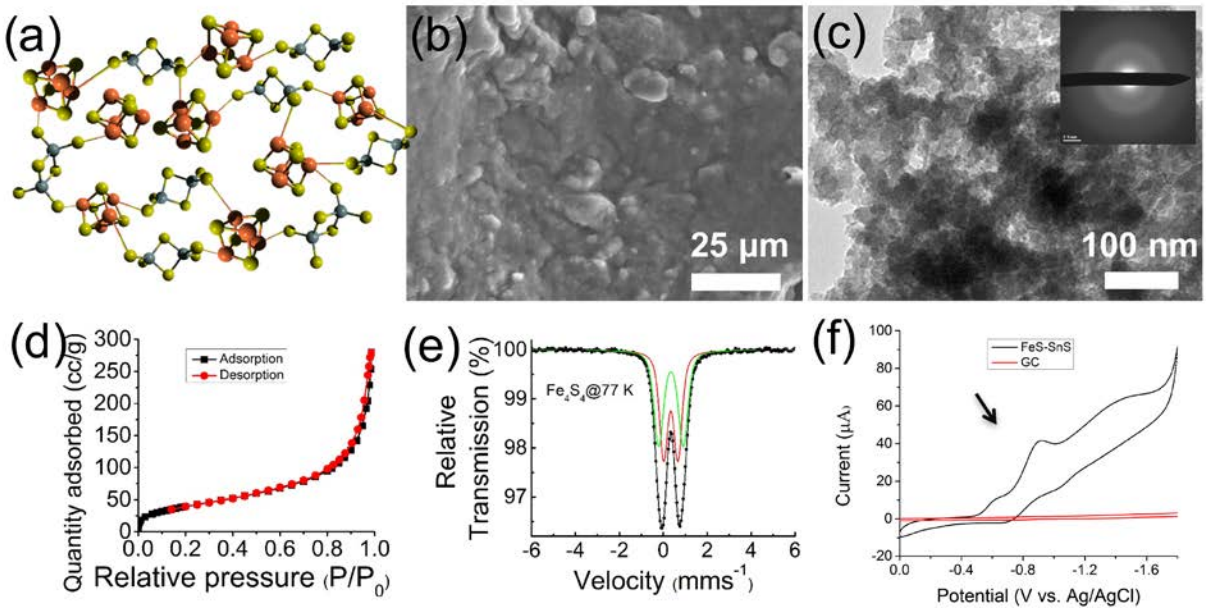

Figure S5. a) The schematic chalcogel network consisting of $(Ph_4P)_2[Fe_4S_4Cl_4]$ and the linking agent $Sn_2S_6^{4-}$; (b) SEM image of FeS-SnS chalcogel. (c) TEM image of Fe_4S_4 chalcogel with the insets showing TEM SEAD pattern images. (d) Nitrogen adsorption/desorption isotherms obtained at 77 K of FeS-SnS aerogel. (e) Mössbauer spectrum of the FeS-SnS chalcogel recorded at 77 K. (f) Cyclic voltammetry of FeS-SnS chalcogel at 50 mV/s scan rate with first reduction peak at -0.91 V.

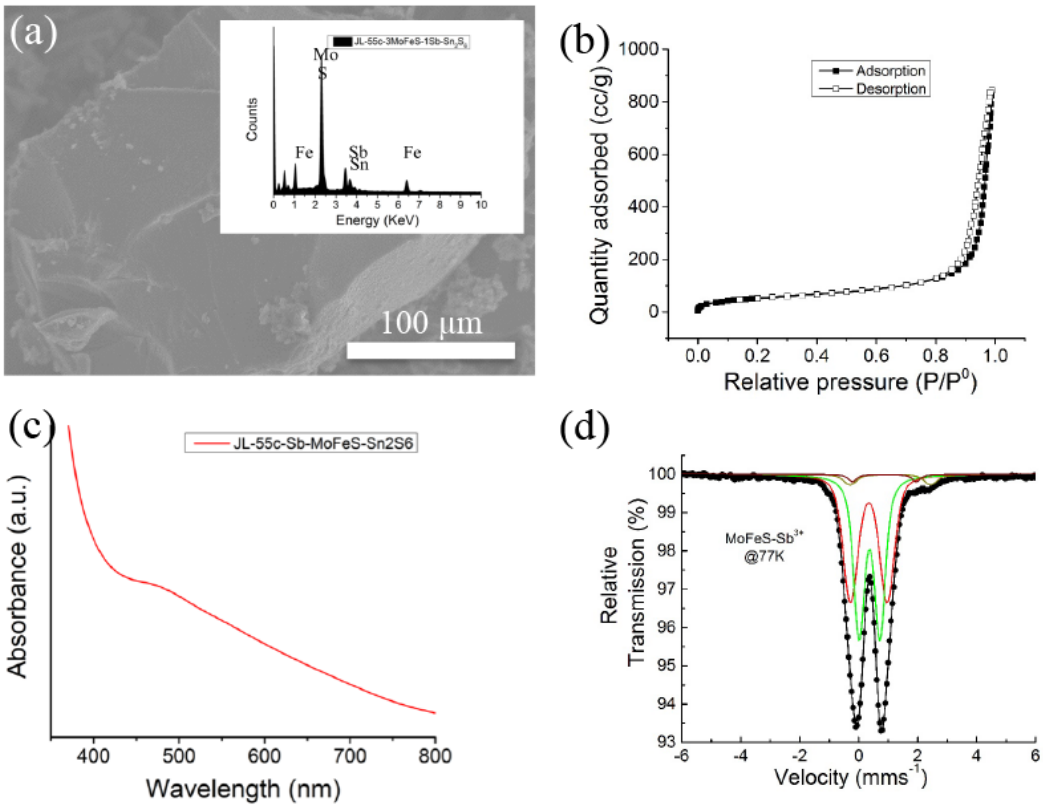

Figure S6. FeMoS-Sb-SnS chalcogel characterizations. (a) SEM images with EDX in the inset. (b) N_2 adsorption-desorption isotherms of FeMoS-Sb-SnS aerogel. (c) UV-vis spectrum of FeMoS-Sb-SnS chalcogel that have been exposed to excess of benzenethiol. (d) Mössbauer spectrum of the FeMoS-Sb-SnS aerogel recorded at 77K.

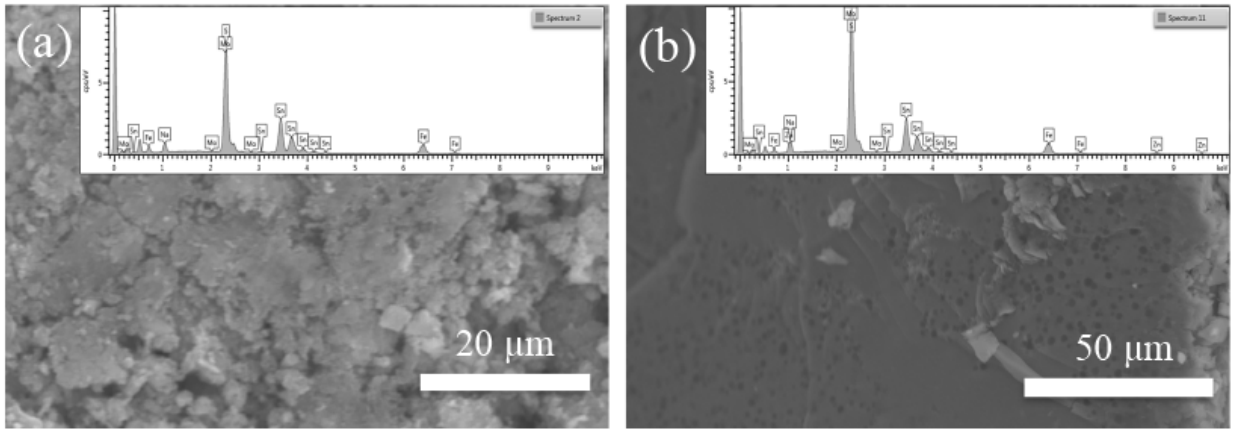

Figure S7. SEM and EDX characterizations of FeMoS-Sn-SnS (a) and FeMoS-Zn-SnS (b) chalcogels, respectively.

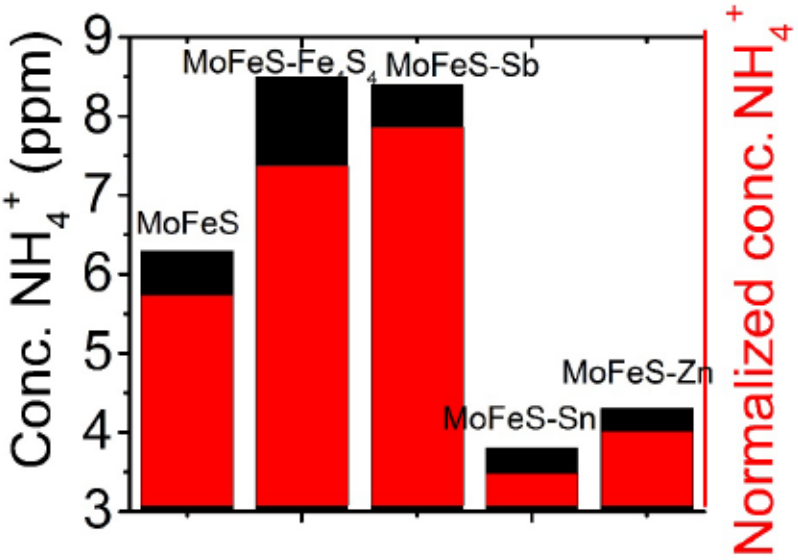

Figure S8. Photocatalytic N_2 reduction performance comparisons for FeMoS-M-SnS Chalcogels.

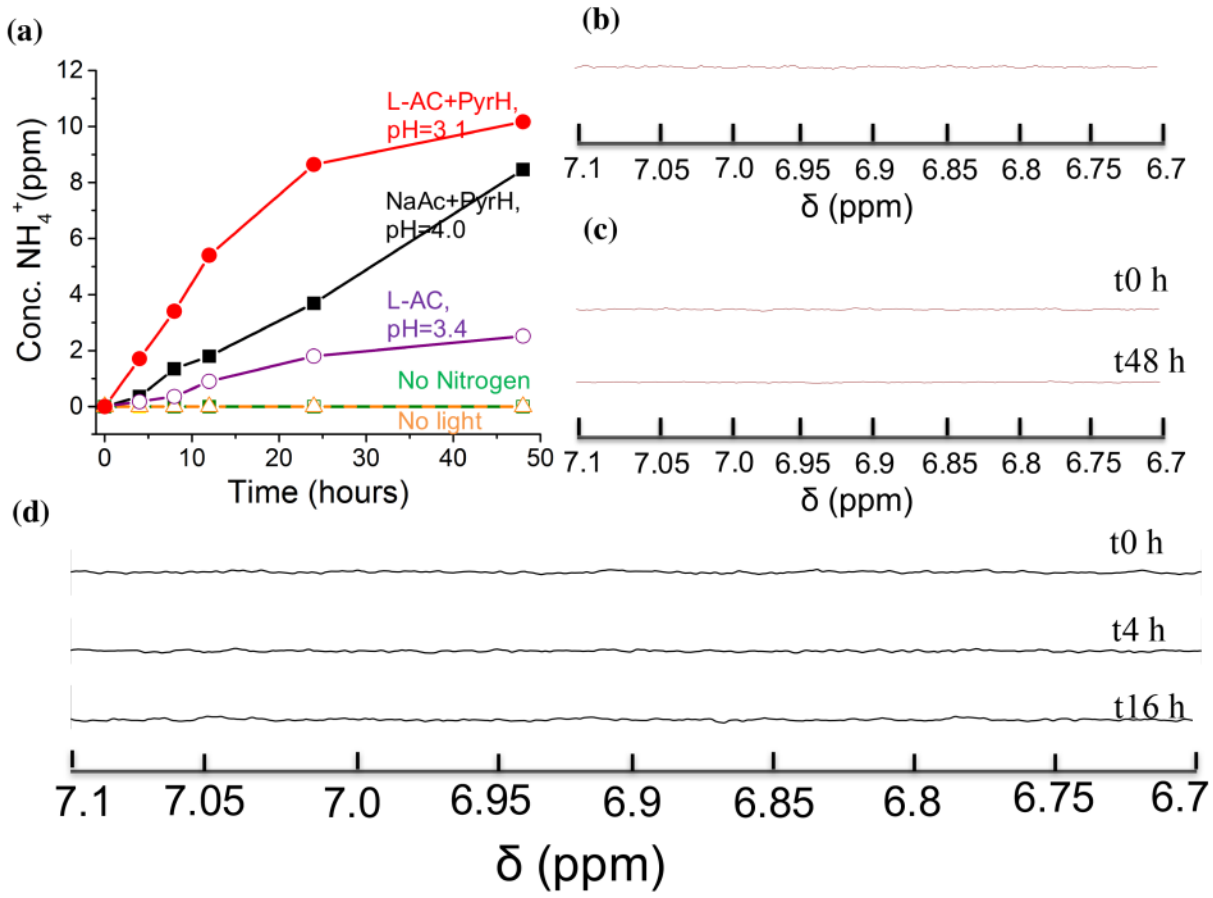

Figure S9. (a) The N_2 fixation kinetics over FeMoS-FeS-SnS chalcogels for a set of control and optimum reaction conditions. L-AC: L-Ascorbic acid; NaAc: Sodium Ascorbate; PyrH: pyridinium hydrochloride. (b) ^{1}H NMR spectra of ultrapure H_2O showing absence of adventitious NH_3 (this water was employed in all our experiments). (c) ^{1}H NMR spectra of the experiment containing all ingredients (FeMoS-FeS-SnS chalcogels, Sodium Ascorbate; pyridinium hydrochloride) but conducted in the dark. (d) ^{1}H NMR spectra of a control experiment with $Na_4Sn_2S_6$ replacing FeMoS-FeS-SnS chalcogels under standard N_2 reduction conditions (Sodium Ascorbate 10 mg; pyridinium hydrochloride 55 mg; N_2 flow; H_2O 10 ml).

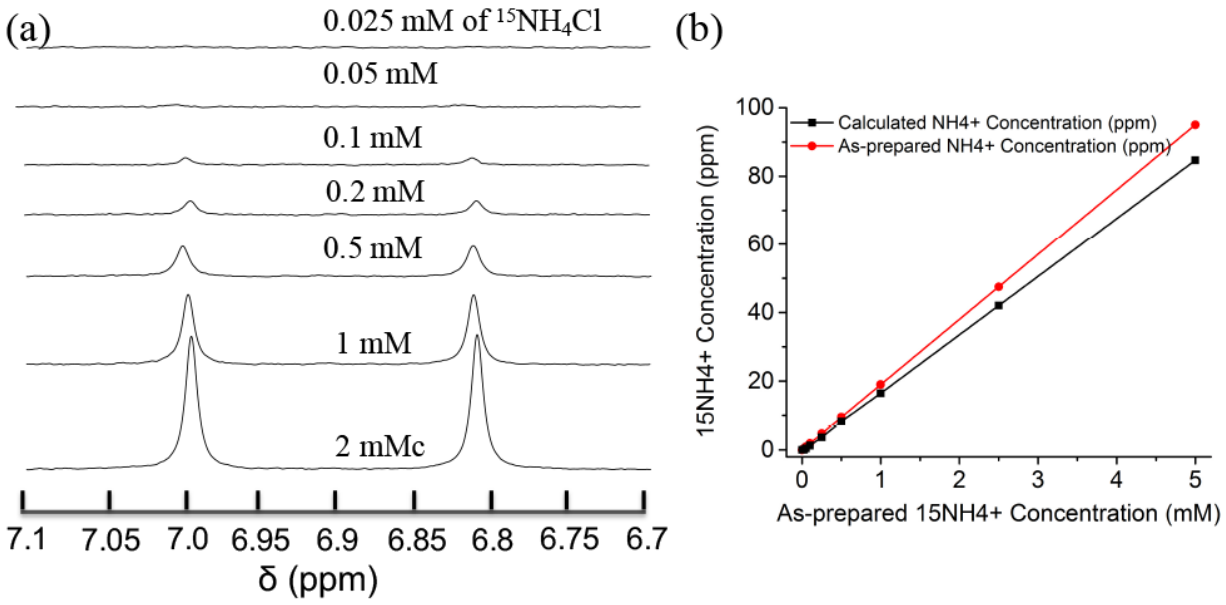

Figure S10. ^{1}H NMR of a $^{15}NH_4Cl$ standard sample used for the calibration curve..

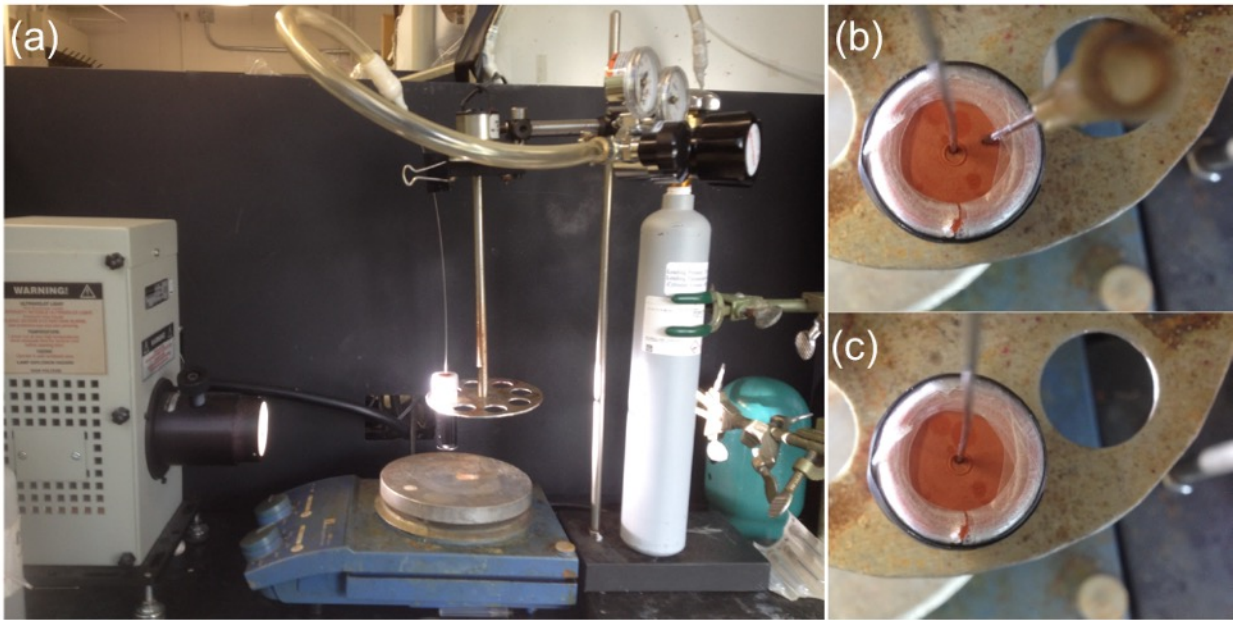

Figure S11. (a) Photocatalytic setup for ^{15}N isotopic labelling experiment with irradiation from Xenon lamp; (b) the outlet needle was present to purge the solution with continuous gas flow; (c) after purging with helium and $^{15}N{\equiv}^{14}N$, consecutively, the outlet was removed and $^{15}N{\equiv}^{14}N$ pressure was built up for running reaction.

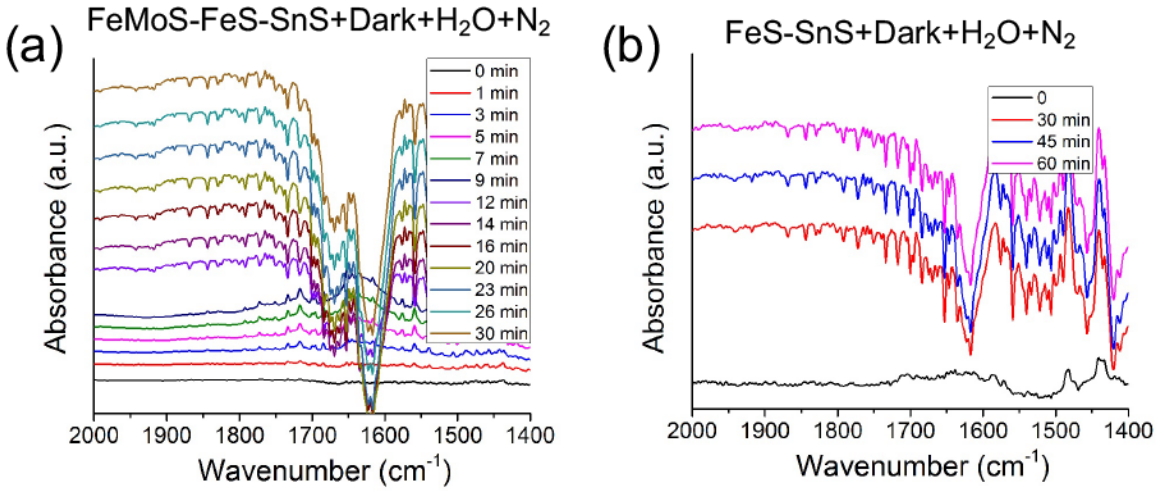

Figure S12. DRIFTS spectra of FeMoS-FeS-SnS with H_2O and $^{14}N_2$ in the absence of light irradiation (a); FeS-SnS aerogel with D_2O and $^{14}N_2$ in the absence of light irradiation (b).

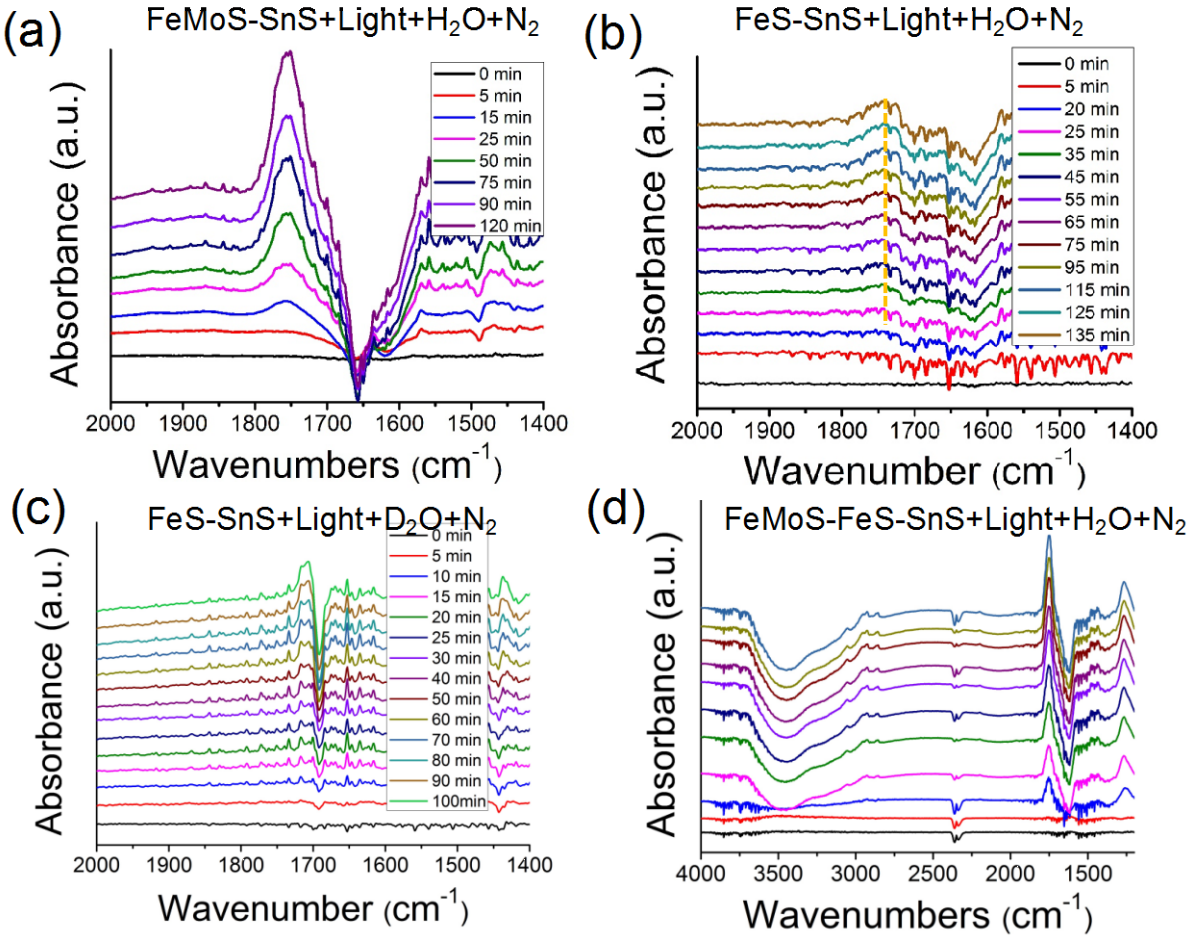

Figure S13. DRIFTS spectra of FeMoS-SnS with H_2O and $^{14}N_2$ in the presence of light irradiation (a); FeS-SnS aerogel with H_2O and $^{14}N_2$ in the presence of light irradiation (b); (c) FeS-SnS aerogel with D_2O and $^{14}N_2$ in the presence of light irradiation; (d) Full-scale DRIFTS spectrum of FeMoS-FeS-SnS (corresponding to **Figure 5b** in main context) with H_2O and $^{14}N_2$ flow collected under light irradiation.

Table S4. Energies of electron and proton sources optimized the same level as described earlier for the broken symmetry DFT calculations.

Species	Energy (hartree)
Ascorbate	-685.349638198351
Ascorbate (Neutral Radical)	-685.1805441
Pyridinium	-249.0558625
Pyridine	-248.5976229

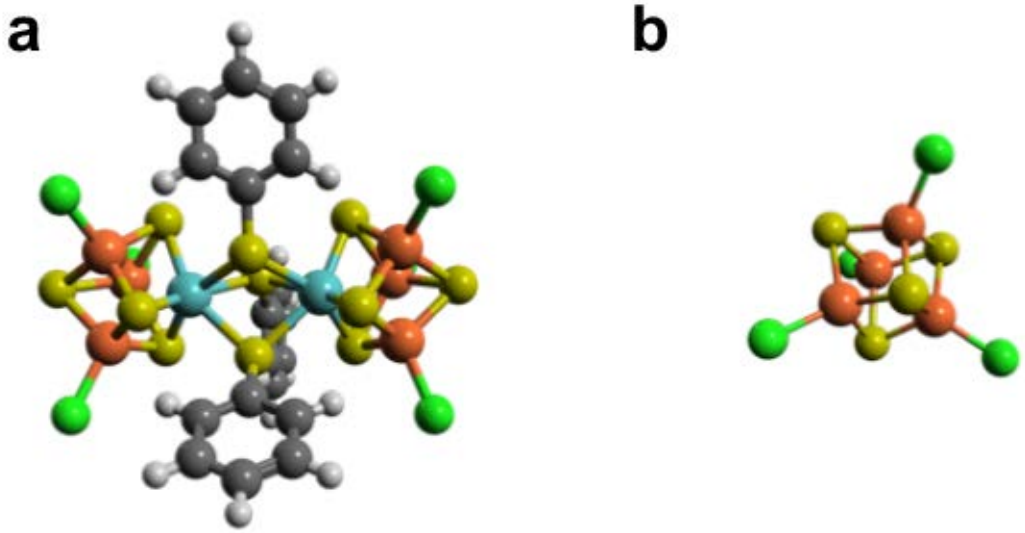

Figure S14. (a) Optimized geometry of model compound $[Mo_2Fe_6S_8(SPh)_3Cl_6]^{3-}$. (b) Optimized geometry of model compound $[Fe_4S_4Cl_4]^{2-}$. Mo = teal, Fe = orange, S = yellow, C = gray, H = white, and Cl = green.

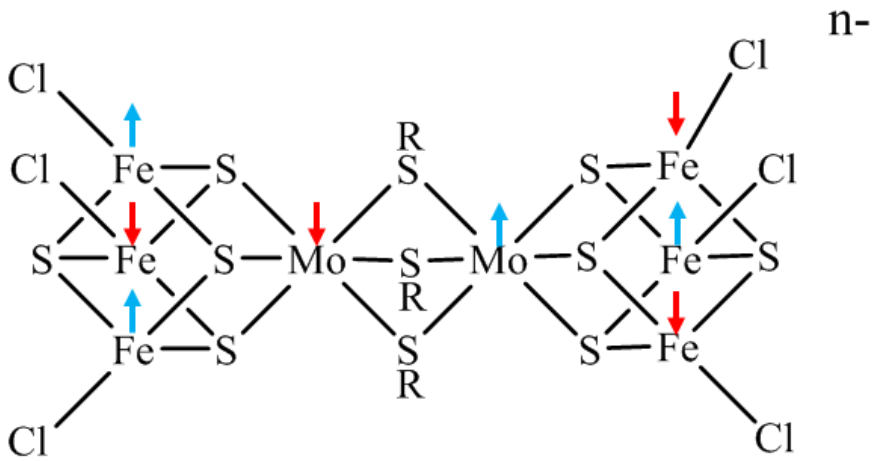

Figure S15. Combination of spin flips of the model complex that lead to the lowest energy broken symmetry DFT solution. Red arrows above a metal atom indicate that its spins were flipped during the calculation. Blue arrows above a metal atom indicate that its spins were undisturbed during the calculation. Such a combination of flips leads to antiferromagnetic coupling between the two cubanes for even total number of electrons, or when n = 3 or n = 5.

Reference

1 Yuhas, B. D. *et al.* Biomimetic multifunctional porous chalcogels as solar fuel catalysts. *J. Am. Chem. Soc.* **133**, 7252-7255 (2011).

2 Kuriyama, S. *et al.* Catalytic Formation of Ammonia from Molecular Dinitrogen by Use of Dinitrogen-Bridged Dimolybdenum-Dinitrogen Complexes Bearing PNP-Pincer Ligands: Remarkable Effect of Substituent at PNP-Pincer Ligand. *J. Am. Chem. Soc.* **136**, 9719-9731 (2014).

3 Banerjee, A. *et al.* Photochemical Nitrogen Conversion to Ammonia in Ambient Conditions with FeMoS-Chalcogels. *J. Am. Chem. Soc.* **137**, 2030-2034 (2015).
4 Barton, E. E., Rampulla, D. M. & Bocarsly, A. B. Selective solar-driven reduction of CO_2 to methanol using a catalyzed p-GaP based photoelectrochemical cell. *J. Am. Chem. Soc.* **130**, 6342-6344 (2008).
5 Lessio, M. & Carter, E. A. What is the role of pyridinium in pyridine-catalyzed CO_2 reduction on p-GaP photocathodes? *J. Am. Chem. Soc.* **137**, 13248–13251 (2015).
6 Lim, C.-H., Holder, A. M. & Musgrave, C. B. Mechanism of homogeneous reduction of CO_2 by pyridine: Proton relay in aqueous solvent and aromatic stabilization. *J. Am. Chem. Soc.* **135**, 142-154 (2012).
7 Mascharak, P. *et al.* Electronic properties of single-and double-$MoFe_3S_4$ cubane-type clusters. *Inorg. Chem.* **22**, 2851-2858 (1983).
8 Tao, J., Perdew, J. P., Staroverov, V. N. & Scuseria, G. E. Climbing the density functional ladder: Nonempirical meta–generalized gradient approximation designed for molecules and solids. *Phys. Rev. Lett.* **91**, 146401 (2003).
9 Weigend, F. & Ahlrichs, R. Balanced basis sets of split valence, triple zeta valence and quadruple zeta valence quality for H to Rn: design and assessment of accuracy. *Phys. Chem. Chem. Phys.* **7**, 3297-3305 (2005).
10 Pantazis, D. A., Chen, X.-Y., Landis, C. R. & Neese, F. All-electron scalar relativistic basis sets for third-row transition metal atoms. *J. Chem. Theory Comput.* **4**, 908-919 (2008).
11 Neese, F., Wennmohs, F., Hansen, A. & Becker, U. Efficient, approximate and parallel Hartree–Fock and hybrid DFT calculations. A 'chain-of-spheres' algorithm for the Hartree–Fock exchange. *Chem. Phys.* **356**, 98-109 (2009).
12 Kossmann, S. & Neese, F. Comparison of two efficient approximate Hartee-Fock approaches. *Chem. Phys. Lett.* **481**, 240-243 (2009).
13 Izsák, R. & Neese, F. An overlap fitted chain of spheres exchange method. *J. Chem. Phys.* **135**, 144105 (2011).
14 van Lenthe, E., Baerends, E.-J. & Snijders, J. G. Relativistic regular two-component Hamiltonians. *J. Chem. Phys.* **99**, 4597-4610 (1993).
15 van Wüllen, C. Molecular density functional calculations in the regular relativistic approximation: Method, application to coinage metal diatomics, hydrides, fluorides and chlorides, and comparison with first-order relativistic calculations. *J. Chem. Phys.* **109**, 392-399 (1998).
16 Klamt, A. & Schüürmann, G. COSMO: a new approach to dielectric screening in solvents with explicit expressions for the screening energy and its gradient. *J. Chem. Soc., Perkin Trans. 2*, 799-805 (1993).
17 Grimme, S. Semiempirical GGA-type density functional constructed with a long‐range dispersion correction. *J. Comput. Chem.* **27**, 1787-1799 (2006).
18 Grimme, S., Antony, J., Ehrlich, S. & Krieg, H. A consistent and accurate ab initio parametrization of density functional dispersion correction (DFT-D) for the 94 elements H-Pu. *J. Chem. Phys.* **132**, 154104 (2010).
19 Srinivas, B. *et al.* Photocatalytic Synthesis of Urea from in situ Generated Ammonia and Carbon Dioxide. *Photochem. Photobiol.* **88**, 233-241 (2012).